ADVANCED MATERIALS
www.advmat.de

Direct Probing of Nanodimensioned Oxide Multilayers with the Aid of Focused Ion Beam Milling

Yener Kuru, Helia Jalili, Zhuhua Cai, Bilge Yildiz,* and Harry L. Tuller**

Recent advances in complex oxide thin film synthesis techniques such as pulsed laser deposition (PLD) and oxide molecular beam epitaxy have stimulated the investigation of novel electronic, magnetic, and ionic properties enabled by the fabrication of superlattices and/or specialized interfaces.[1–12] A prime example of such novel interfacial properties is the high mobility metallic state found to exist at the interfaces of $LaAlO_3$ (LAO)/$SrTiO_3$ (STO) superlattices of below four unit cell thicknesses, while both materials individually are insulating.[13,14] In a second recent example from ionic systems, an eight orders of magnitude enhancement in conductivity in 8 mol% $(Y_2O_3)_x(ZrO_2)_{1-x}$ (YSZ), a standard solid electrolyte used in fuel cells and sensors, was reported when YSZ was integrated within a YSZ/STO superlattice.[15] While the ionic or electronic nature of this conductivity enhancement remains debatable,[16,17] it is reasonable to assume that the strain and/or the defective structure created at the YSZ/STO interfaces likely plays a key role in inducing the large jump in conductivity. As a final example here, the reconstruction of Cu and Mn orbitals adjacent to the interfaces in $La_{0.67}Ca_{0.33}MnO_3/YBa_2Cu_3O_7$ multilayers resulted in antiferromagnetic coupling of Mn and Cu spins.[18]

Interface-driven properties commonly begin to dominate over bulk properties as the multilayer dimensions approach the nanometer scale. A key challenge is how to directly extract properties that are confined to these interfaces while retaining the integrity of the overall structure. While scanning probe methods, in principle, offer the requisite high spatial resolution, there have been challenges in successfully applying these methods to obtain information representative of the structural and electronic states of oxide superlattices.[19–21] For example, as shown in ref. [19], cleaving a single crystal followed by cross-sectional scanning tunneling microscopy (STM) is able to examine the monolayers of the exposed SrO and TiO_2 planes of a STO single crystal on the fracture surface. On the other hand, such a cleavage method for a heterolayer system (made of dissimilar materials) does not controllably expose the heterointerfaces and does not enable the approach of the STM tip onto the real interfaces given the steep slope of the interfacial fracture surface vertical to the scanning direction. The fracture approach was successfully applied to semiconducting InAs/GaSb superlattices due to a relatively large total thickness (i.e., 2 μm) and the existence of (110) easy cleavage planes perpendicular to the initial substrate surface.[22] In ref. [20], a four unit-cell thick LAO thin film was deposited onto STO, forming a single-layer heterostructure. The LAO film surface was then probed by STM and scanning tunneling spectroscopy (STS) to identify the electronic density of states at the LAO/STO interface. One can argue that this approach actually does not reach the interface states and determines the electronic structure only indirectly. Lastly, in ref. [21], a LAO film on a STO substrate was cut cross-sectionally, and the two LAO sides were glued to each other (i.e., similar to cross-sectional transmission electron microscopy specimen preparation) to enable a stable structure under the scanning probe. Both resistance and morphology mapping were carried out employing conducting-tip atomic force microscopy (AFM). The applicability of this method to superlattices with a small modulation length is questionable. Specimens are highly prone to contamination during specimen preparation. Moreover, the glue is a limitation for high-temperature scanning probe measurements,[23,24] important for identifying, in situ, the interface atomic and electronic structure of layered solid oxide fuel cell materials.[5,25,26] Therefore, a general and practical method enabling the local measurements of the structural, electronic, and magnetic properties of buried interfaces in oxide superlattices remains lacking. Here, we demonstrate how such buried interlayers within complex oxide multilayers can be exposed to ambient conditions by focused ion beam (FIB) milling by employing a small incidence angle between the specimen surface and the ion beam. The advantages of this novel method include the capability for directly exposing the interfaces of a multilayer system in a geometry feasible for scanning probe measurements, and the capability for controlling the vertical and lateral dimensions and crystallographic orientations of the layers so exposed.

The $La_{0.65}Sr_{0.35}MnO_3$ (LSM)/$SrTi_{0.2}Fe_{0.8}O_3$ (STF) multilayer was selected to illustrate the proposed FIB-based method. LSM is the standard cathode material used in high-temperature solid oxide fuel cells[23] while STF, due to its high mixed electronic and ionic conductivities (MIEC), is a promising cathode material for intermediate-temperature fuel cells.[27] The multilayer exhibits the best features of each cathode material, given the much higher electronic conductivity of LSM, which is advantageous for minimizing current collection losses, and MIEC of STF promising reduced overpotentials. Owing to their distinctly different electronic and magnetic properties (LSM is ferromagnetic at ambient temperature),[27–31] they can be readily

Dr. Y. Kuru, Dr. H. Jalili, Dr. Z. Cai, Prof. B. Yildiz
Department of Nuclear Science and Engineering
Massachusetts Institute of Technology
77 Massachusetts Avenue
Cambridge, MA 02139, USA
E-mail: ykuru@mit.edu; byildiz@mit.edu
Dr. Y. Kuru, Prof. H. L. Tuller
Department of Materials Science and Engineering
Massachusetts Institute of Technology
77 Massachusetts Avenue
Cambridge, MA 02139, USA
E-mail: tuller@mit.edu

DOI: 10.1002/adma.201102401

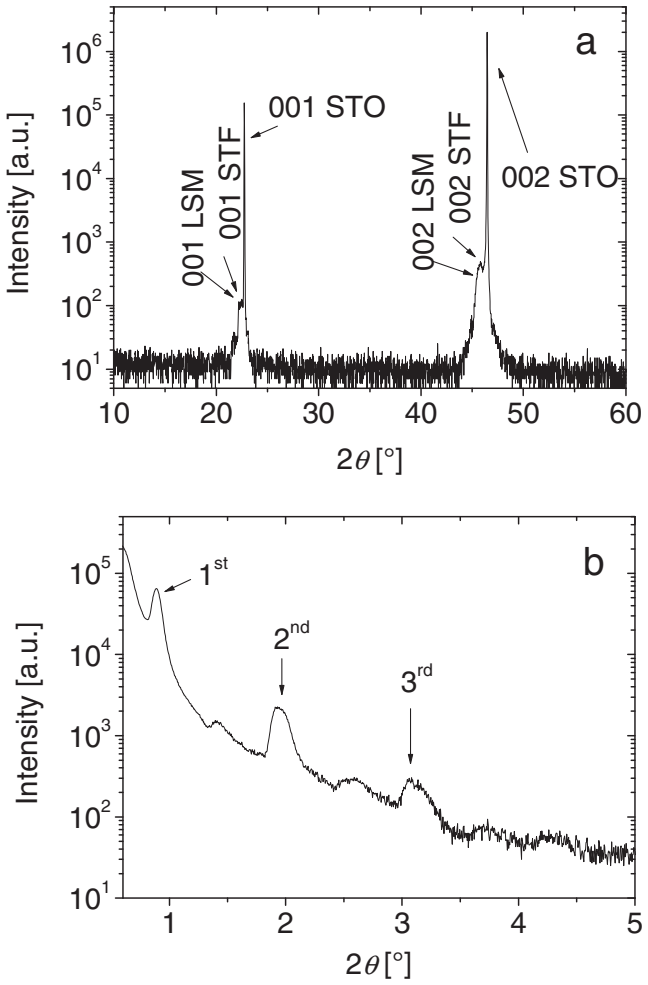

Figure 1. a) The $2\theta - \omega$ scan between 10° and 60°, showing the 001 and 002 reflections of the layers and the substrate. b) The low-angle diffraction pattern of the multilayer indicating the first three superstructure peaks due to periodicity of the multilayer.

distinguished in a heterolayer configuration by STM, STS, and magnetic force microscopy (MFM).

A LSM/STF multilayer, deposited onto a STO single crystal substrate by PLD (see Experimental Section), was characterized by high-resolution X-ray diffraction measurements. The long-range and low-angle $2\theta - \omega$ scans of the multilayer, where 2θ is the angle between the incident and the diffracted X-ray beams and ω is the angle between the incident beam and the specimen surface, are presented in **Figure 1**a,b, respectively. The former shows that only 00*l* reflections of both materials are present in the diffraction pattern; no peaks from any other impurity phase or orientation were observed. Since the bulk lattice parameters of both layers are smaller than the lattice parameter of STO, the out-of-plane lattice parameters of the layers on STO substrate would be expected to be even smaller. However, as seen in Figure 1a, the out-of-plane lattice parameters of the layers are larger than that of the substrate. This may be an indication of O loss from the layers and an accompanying expansion.[32] The first three superstructure peaks resulting from the multilayer periodicity are seen in Figure 1b. These three peaks indicate that the modulation length, Λ, of the multilayer (i.e., $\Lambda = t_{LSM} + t_{STF}$) is approximately 10 nm.

The low incidence angle (α) FIB milling process designed to expose the layer cross section at a specified orientation is shown schematically in **Figure 2**a. Milling with a shallow angle, α, results in an effective magnification of the very thin layers of the superlattice by a factor of $1/\sin\alpha$. This forms a new surface with α degrees inclined from the original film surface (Figure 2b). The original thickness of each layer, h_1 and h_2, is magnified by a factor of $1/\sin\alpha$ on this surface, exposing a lateral width of $h_1/\sin\alpha$ and $h_2/\sin\alpha$. In addition, in the FIB-exposed region, the thickness of each exposed layer varies spatially from its nominal thickness, h_1 or h_2 at the beginning of each successive layer to 0 at the end of that layer (see the points 1 and 2, respectively, for an innner LSM layer in Figure 2c,d). An advantage of this method is that it enables one to consistently form an array of exposed layers with gradually varying thickness. At the same time, the layer structure is conserved across nearly the entire sample with only the exposed regions exhibiting a varying thickness from one heterointerface to the next due to the grazing incidence FIB-cut of the edge of the multilayer structure. For example, this provides a means for determining the critical thickness at which a 2D electron gas is formed in such multilayer systems,[13,14] by scanning the STM tip along the inclined edge of the FIB-cut region. Furthermore, multiple multilayer structures with different nominal layer thicknesses (varying h_1 and h_2) can be deposited and investigated in comparison to each other, while being able to probe the conductivity of each individual interface (by contacting the interface with two probes on both ends of the structure).

Figure 3 is a low-magnification atomic force microscopy (AFM) image of the FIB-cut surface; the top surface LSM layer is also seen in Figure 3. It is evident that the morphologies of the inner LSM layers and the surface LSM layers are both granular. On the other hand, the STF layer cross sectional surfaces are quite smooth. There is a transition region between the LSM and STF layers for which the apparent grain or hillock size becomes smaller and smaller while approaching the STF layer.

MFM measurements were performed on the specimen at ambient conditions. Although the Curie temperature (T_C) of bulk LSM is known to be slightly above room temperature,[30] no ferromagnetic signal could be observed for this multilayer specimen at room temperature. This result is indeed consistent with the recent results reported by Kim et al. regarding the suppression of T_C with decreasing layer thickness.[30]

The AFM and STM images of the multilayer are illustrated in **Figure 4**a,b with the corresponding height profiles perpendicular to the interfaces of the layers (i.e., shown by rectangles in Figure 4a,b). AFM line scans show little surface roughness in the STF; the root mean square roughness value is less than 1 nm, which is inline with the gentle FIB milling process (see Experimental Section). On the other hand, the LSM layers do exhibit the roughness already described in the low-magnification AFM image of Figure 3, showing periodic perturbations roughly ±2 nm relative to the flat STF surface. It is worth noting that the cross-sectional width exposed for each layer is approximately 500 nm following the FIB milling (see Figure 4a),

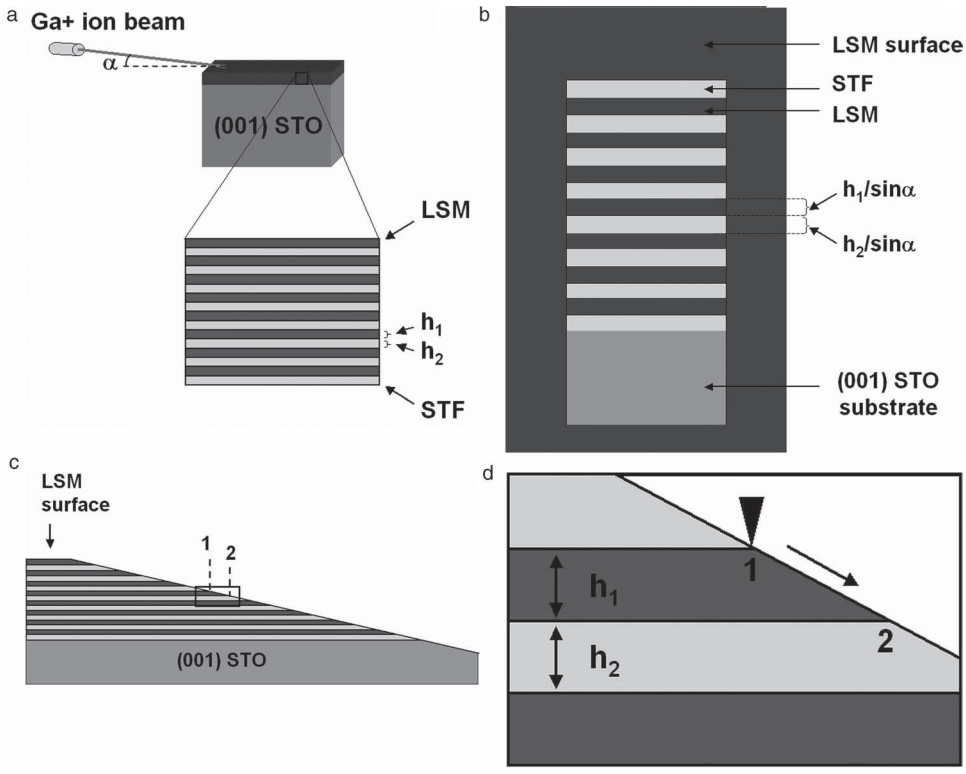

Figure 2. a) Schematic description of the FIB milling process with a shallow incidence angle, α, allowing to expose and visualize the inner layers and the interfaces. b) The top view of the multilayer specimen after FIB milling. The thickness of each layer, h_1 and h_2, is magnified by a factor of 1/sin α, exposing a lateral width of h_1/sin α and h_2/sin α. c) The cross-sectional view of the multilayer after the FIB milling, illustrating the spatial variation of the layer thicknesses for the newly formed surface. The thickness of each of the inner LSM layers varies from h_1 to 0, as examplified from point 1 to point 2. d) The enlarged view of the cross section shown in (c), illustrating the thickness variation in the layers, exemplified from 1 to 2 in an LSM layer, during scanning the FIB milled region.

while the deposited thickness of the layers vertical to the substrate is about 10 nm per pair of layers. Compared to the AFM line scans, the STM line scans (Figure 4c) show substantially larger height variations, reaching nearly 10 nm between the consecutive layers. Consistent with this, the LSM layer with granular morphology and the transition region appear bright whereas STF layers look darker on the STM image (Figure 4b). The "topography" probed with AFM is the real topography, while the "topography" probed with STM is a convolution of the actual topography with the electronic states of the material. Therefore, this image-contrast difference betweem STM and AFM height profiles must have an electronic origin. The STM tip should approach the surface more closely to reach the set feedback tunneling current for the less conducting STF layer and this is reflected as a height difference in the line scan. Furthermore, the STM height profile does not exhibit a step function across the layers, but rather shows a continuous variation of apparent "height" from the center of the layers to their heterointerfaces. This suggests that, at least for the STF layers, the electronic structure is influenced by the neighboring LSM layers in this model system. The bandgap values (i.e., 0.3 and 1 eV for LSM and STF, respectively) derived from the tunneling spectra (Figure 4d) are consistent with this observation and are considerably smaller than the reported values for their bulk counterparts (i.e., ≈1 eV and ≈2 eV for LSM and STF, respectively[28,31]). One or both of the following possibilities could be the source of these observations: i) the proximity of the layers may alter the electronic structures of both components near the interfaces by modifying the bonding state of the atoms and/or

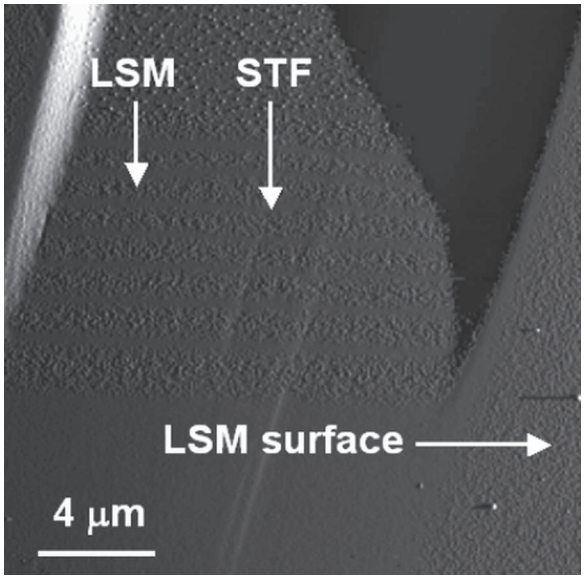

Figure 3. Low-magnification AFM image of the FIB-cut multilayer. The top LSM layer and the inner LSM and STF layers are shown by arrows.

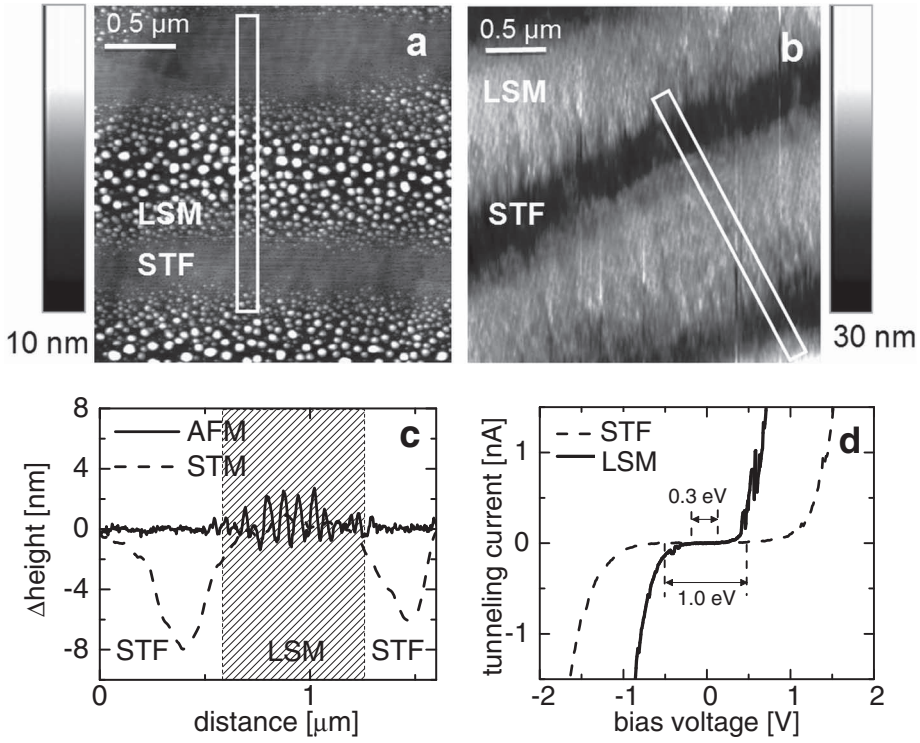

Figure 4. a) AFM and b) STM images of the FIB-cut cross-section of the LSM/STF multilayer. c) AFM and STM height profiles of the FIB-cut cross-sections in (a) and (b). The rectangles in (a) and (b) show the regions where the height profiles are taken from. The height differences are given relative to the starting points of the profiles. d) Tunneling current as a function of bias voltage for the LSM and STF layers.

ii) the modifications in the electronic and magnetic properties may have a structural origin, e.g., strain or high defect densities created at the interfaces.[33]

It is worth nothing that the FIB milling method can result in ion irradiation induced damage in the material; a well known challenge to specimen preparation in various microscopy techniques. The depth of the collision cascade upon ion bombardment depends on several factors including beam energy, incidence angle and material being bombarded. Various types of defects (e.g. amorphized regions, point defects, defect clusters and dislocation loops) can be generated in the collision cascade volume during FIB milling; the type and concentration of these defects are also time and temperature dependent.[34,35] In this work, it is evident from Figure 3 that amorphization is likely not present in our samples given that the LSM top surface (not subject to FIB milling) and the inner LSM layers (exposed to FIB milling) exhibit the identical nano-granular morphology (see Figure 3 and Figure 4a). Our FIB-exposed LSM layers possess grain boundaries and therefore cannot be amorphous. Furthermore, the measured band gap values of the LSM and STF regions are distinctly different from each other and consistent with the more conducting behaviour of LSM (see Figure 4c,d). Finally, the concentration of Ga^+ ions implanted in the near-surface region of the FIB-cut region was measured by nano-probe Auger electron spectroscopy (AES) and is found to be about 1%. Such a low Ga concentration is unlikely to cause drastic structural changes like amorphization. The absence (or relatively small fraction) of an amorphous region in our materials can be attributed to a combination of the low incidence angle (i.e. less than 1°), relatively low ion current (i.e. approximately 100 pA) and the robust oxides used. Even in the event that an amorphous layer were formed at the exposed regions, this would not limit the applicability of this method since such layers could easily be removed by one (or a combination) of methods such as a brief etch, low energy ion milling and thermal annealing following FIB milling,[36] but prior to the scanning probe measurements of the local properties of the interfaces and layers.

In conclusion, the inner layers and interfaces of the LSM/STF multilayer structure were exposed to ambient conditions and examined in this study by AFM, MFM, STM, and STS following FIB milling. A number of interesting features were observed that were previously not accessible in an integrated manner. The surface morphology showed a transition from granular to smooth while shifting from LSM to STF. The electronic properties of LSM and STF were shown to be modified compared to bulk properties, depending on the proximity to the STF/LSM interface, on the basis of the bandgap values obtained from the STS data, STM images, and height profiles. In addition, the LSM layers were found not to be ferromagnetic at ambient conditions, contrary to what is observed in their bulk state.

As demonstrated in this work, it is now possible to reach the inner layers and interfaces of complex oxide multilayers by FIB milling, employing a small and controlled angle of incidence. This, for the first time, enabled high-resolution and

coordinated measurement of the structural, electrionic, and magnetic properties of individual layers and interfaces in multilayer oxides. An important feature of this method is its generality, which enables it to be applied to a much broader range of material systems and conditions when compared to other previously reported methods. Furthermore, it provides a platform for investigating important characteristics of layered systems, for example size effects, or properties as a function of distance from the interfaces, due to the effective spatial magnification that this method grants.

Experimental Section

Film Deposition: The LSM/STF multilayer was deposited on a (001) STO single crystal substrate by PLD using a KrF excimer laser that emits at 248 nm. The energy per pulse, repetition rate, and target to substrate distance were 400 mJ per pulse, 8 Hz, and 8 cm, respectively. After reaching a background pressure of 10^{-5} mbar, the layers were consecutively deposited at 700 °C under 0.01 mbar O_2 pressure. Thereafter, the multilayer was cooled to room temperature under an O_2 pressure of 10 mbar to complete the oxidation of the films. The thickness of both layers (nominal thickness of LSM and STF ≈5 nm) was adjusted by the deposition rate, which was determined by calibration depositions. The LSM/STF bilayer was repeated 8 times. STF was the first layer on the STO substrate, whereas the LSM was the top layer of the superlattice.

XRD Measurements: The $2\theta - \omega$ scans were performed employing a high-resolution four-circle Bruker D8 Discover diffractometer, equipped with a Göbel mirror, 4-bounce Ge (022) channel-cut monochromator, Eulerian cradle, and a scintillation counter, using Cu $K\alpha_1$ radiation.

FIB Milling Process: The FIB milling process was carried out by a Helios Nanolab 600 dual beam FIB milling system. The Ga+ ion current and accelerating voltage were 100 pA and 30 kV, respectively. The specimen was mounted carefully to the sample holder by carbon tape and the incidence angle was set to 5°. However, the actual incidence angle was below 1° due to a slight misalignment of the specimen during mounting onto the carbon tape (Figure 4a; each layer was ≈500 nm thick after FIB milling).

AFM, MFM, STM, and STS Measurements: A Veeco Digital Instrument Nanoscope IV was used to characterize the surface morphology, electronic, and magnetic structure. In order to study the surface morphology, AFM was used in tapping mode, employing a commercial phosphorus doped Si tip. MFM measurement was performed by a Co-coated Cr magnetic tip in a lift mode (50 nm) to determine the magnetic signal arising from the multilayer structure. Scanning tunnelling microscopy was performed at room temperature in ambient conditions using a chemically etched Pt-Ir tip. STM images were obtained in constant current mode with bias voltage and current set to 0.5 V and 500 pA, respectively.

AES Measurements: A Physical Electronics Model 700 scanning nanoprobe Auger electron spectrometer was used to identify the near-surface Ga content with high spatial resolution. Incident electrons of 10 keV and 10 nA were used, and smoothing and differentiation of the AES spectra collected were carried out using the Savitsky–Golay algorithm. Quantification of AES differential spectra was performed using peak-to-peak intensities of the tight scans of different elements (e.g., O, La, Sr, Mn, Ga, Ti, and Fe).

Acknowledgements

This research was funded by the MIT Energy Initiative Seed Fund Program and the Basic Energy Sciences, Department of Energy under award DE SC0002633. The FIB milling process and X-ray diffraction, STM, AFM, and MFM measurements were performed at MIT's Center of Materials Science and Engineering, an NSF MRSEC facility.

Received: June 24, 2011
Revised: July 27, 2011
Published online: September 8, 2011

[1] J. Chakhalian, J. W. Freeland, H. U. Habermeier, G. Cristiani, G. Khaliullin, M. van Veenendaal, B. Keimer, *Science* **2007**, *318*, 1114.
[2] A. Gozar, G. Logvenov, L. Fitting Kourkoutis, A. T. Bollinger, L. A. Giannuzzi, D. A. Muller, I. Bozovic, *Nature* **2008**, *455*, 782.
[3] Z. Sefrioui, M. Varela, V. Pena, D. Arias, C. Leon, J. Santamaria, J. E. Villegas, J. L. Martinez, W. Saldarriaga, P. Prieto, *Appl. Phys. Lett.* **2002**, *81*, 4568.
[4] G. Logvenov, A. Gozar, I. Bozovic, *Science* **2009**, *326*, 699.
[5] J. Garcia-Barriocanal, F. Y. Bruno, A. Rivera-Calzada, Z. Sefrioui, N. M. Nemes, M. Garcia-Hernandez, J. Rubio-Zuazo, G. R. Castro, M. Varela, S. J. Pennycook, C. Leon, J. Santamaria, *Adv. Mater.* **2010**, *22*, 627.
[6] T. Y. Chien, J. Liu, J. Chakhalian, N. P. Guisinger, J. W. Freeland, *Phys. Rev. B* **2010**, *82*, 041101(R).
[7] E. Dagotto, *Science* **2007**, *318*, 1076.
[8] J. D. Ferguson, Y. Kim, L. F. Kourkoutis, A. Vodnick, A. R. Woll, D. A. Muller, J. D. Brock, *Adv. Mater.* **2011**, *23*, 1226.
[9] Y. Xie, C. Bell, Y. Hikita, H. Y. Hwang, *Adv. Mater.* **2011**, *23*, 1744.
[10] A. B. Shah, Q. M. Ramasse, X. Zhai, J. G. Wen, S. J. May, I. Petrov, A. Bhattacharya, P. Abbamonte, J. N. Eckstein, J. M. Zuo, *Adv. Mater.* **2010**, *22*, 1156.
[11] X. Zhai, C. S. Mohapatra, A. B. Shah, J. M. Zuo, J. N. Eckstein, *Adv. Mater.* **2010**, *22*, 1136.
[12] K. J. Jin, H. B. Lu, K. Zhao, C. Ge, M. He, G. Z. Yang, *Adv. Mater.* **2009**, *21*, 4636.
[13] A. Ohtomo, D. A. Muller, J. L. Grazul, H. Y. Hwang, *Nature* **2002**, *419*, 378.
[14] A. Ohtomo, H. Y. Hwang, *Nature* **2004**, *427*, 423.
[15] J. Garcia-Barriocanal, A. Rivera-Calzada, M. Varela, Z. Sefrioui, E. Iborra, C. Leon, S. J. Pennycook, J. Santamaria, *Science* **2008**, *321*, 676.
[16] A. Kushima, B. Yildiz, *J. Mater. Chem.* **2010**, *20*, 4809.
[17] N. Schichtel, C. Korte, D. Hesse, J. Janek, *Phys. Chem. Chem. Phys.* **2009**, *11*, 3043.
[18] J. Chakhalian, J. W. Freeland, G. Srajer, J. Strempfer, G. Khaliullin, J. C. Cezar, T. Charlton, R. Dalgliesh, C. Bernhard, G. Cristiani, H. U. Habermeier, B. Keimer, *Nat. Phys.* **2006**, *2*, 244.
[19] N. P. Guisinger, T. S. Santos, J. R. Guest, T. Y. Chien, A. Bhattacharya, J. W. Freeland, M. Bode*ACS Nano* **2009**, *3*, 4132.
[20] M. Breitschaft, V. Tinkl, N. Pavlenko, S. Paetel, C. Richter, J. R. Kirtley, Y. C. Liao, G. Hammerl, V. Eyert, T. Kopp, J. Mannhart, *Phys. Rev. B* **2010**, *81*, 153414.
[21] M. Basletic, J. L. Maurice, C. Carretero, G. Herranz, O. Copie, M. Bibes, E. Jacquet, K. Bouzehouane, S. Fusil, A. Barthelemy, *Nat. Mater.* **2008**, *7*, 621.
[22] Y. Hirayama, T. Sogawa, K. Suzuki, K. Kanisawa, H. Yamaguchi, *Phys. Status Solidi B* **2007**, *244*, 2988.
[23] K. Katsiev, B. Yildiz, K. Balasubramaniam, P. A. Salvador, *Appl. Phys. Lett.* **2009**, *95*, 092106.
[24] H. Jalili, J. W. Han, Y. Kuru, Z. Cai, B. Yildiz, *J. Phys. Chem. Lett.* **2011**, *2*, 801.
[25] N. Sata, K. Eberman, K. Eberl, J. Maier, *Nature* **2000**, *408*, 946.
[26] E. Fabbri, D. Pergolesi, E. Traversa, *Chem. Soc. Rev.* **2010**, *39*, 4355.

[27] W. C. Jung, H. L. Tuller, *J. Electrochem. Soc.* **2008**, *155*, B1194.
[28] K. Zhao, K. Jin, H. Lu, Y. Huang, Q. Zhou, M. He, Z. Chen, Y. Zhou, G. Yang, *Appl. Phys. Lett.* **2006**, *88*, 141914.
[29] V. L. Kozhevnikov, I. A. Leonidov, M. V. Patrakeev, E. B. Mitberg, K. R. Poeppelmeier, *J. Solid State Chem.* **2001**, *158*, 320.
[30] B. Kim, D. Kwon, J. H. Song, Y. Hikita, B. G. Kim, H. Y. Hwang, *Solid State Commun.* **2010**, *150*, 598.
[31] A. Rothschild, W. Menesklou, H. L. Tuller, E. Ivers-Tiffee, *Chem. Mater.* **2006**, *18*, 3651.
[32] Y. Kuru, S. R. Bishop, J. J. Kim, B. Yildiz, H. L. Tuller, *Solid State Ionics,* **2011**, *193*, 1.
[33] A. X. Gray, C. Papp, B. Balke, S. H. Yang, M. Huijben, E. Rotenberg, A. Bostwick, S. Ueda, Y. Yamashita, K. Kobayashi, E. M. Gullikson, J. B. Kortright, F. M. F. de Groot, G. Rijnders, D. H. A. Blank, R. Ramesh, C. S. Fadley, *Phys. Rev. B* **2010**, *82*, 205116.
[34] G. S. Was, *Fundamentals of Radiation Materials Science: Metals and Alloys*, Springer-Verlag, Berlin and Heidelberg, Germany **2007**.
[35] M. Ghaly, R. S. Averback, *Phys. Rev. Lett.* **1994**, *72*, 364.
[36] J. F. Groves, Y. Du, I. Lyubinetsky, D. R. Baer, *Superlattices Microstruct.* **2008**, *44*, 677.